RSC Advances

PAPER

View Article Online
View Journal | View Issue

Cite this: *RSC Adv.*, 2025, **15**, 4774

Controllable synthesis of cypress-derived hard carbon for high-rate sodium ion storage†

Yan Zhou,‡[a] Meixiang Cen,‡[b] Changlin Pan,[a] Jiapeng Hu,[a] Yongqi Liu,[b] Yun Zhang,[b] Wenjie Zhang,[b] Gujie Qian*[c] and Jiabiao Lian *[b]

Received 14th November 2024
Accepted 31st January 2025

DOI: 10.1039/d4ra08080g

rsc.li/rsc-advances

Optimized chemical pretreatment method facilitates the synthesis of biomass-based hard carbon with rich porosity at lower carbonization temps (900–1300 °C), yielding cost-effective and high-performance anode materials. The cypress-derived hard carbon (WC-1100) with hierarchical pores achieves a peak sodium ion storage of 307 mA h g^{-1} at 0.1 A g^{-1} with an impressive ICE of 82.5%.

In the past decade, lithium-ion batteries (LIBs) have experienced a remarkable boom due to their impressive performance and the explosive demand for renewable energy solutions.[1] Nonetheless, their application in large-scale energy storage systems (ESS) remains constrained by high cost and the scarcity of lithium resources.[2,3] Researchers are now focusing attention on sodium-ion batteries (SIBs) as promising candidates for extensive energy storage applications, which have similar electrochemical properties and notably lower material costs than LIBs.[4] Despite the significant advancements made by SIBs, they still lag behind LIBs in terms of energy density.[5] Consequently, identifying electrode materials with enhanced capacities poses a pivotal challenge to drive the ongoing development of SIBs. For instance, the commercial graphite used in LIBs does not work in SIBs on anodes.[6] So, it is critical to select a suitable anode material for SIBs. Different from graphite, hard carbon (HCs) materials with high specific capacities (≈300 mA h g^{-1}) and excellent cost-effectiveness are considered to be the most feasible anode materials of SIBs for further commercialization.[7]

As typical eco-friendly resources, biomass has become a global hot topic of sustainable chemistry due to its great potential for practical application. In recent years, researchers are paying more attention to synthesis of hard carbon *via* abundant biomass-based materials instead of expensive inorganic materials, such as peat moss,[8] grapefruit peel,[9] nutshell,[10] reed straw,[11] cork,[12] and palm fruit calyx.[13] As the annual production of wood wastes by the forestry industry worldwide is massive, the reuse of the wood wastes may be both environmentally and economically sustainable. Furthermore, the unique advantages of wood-derived materials, including their abundance in resources, renewability, sustainability, and cost-effectiveness, make them extremely attractive for electrochemical energy storage, notably in low-cost stationary power grids and portable electronic devices, thereby prompting researchers to delve into the development of high-capacity hard carbon materials sourced from waste wood.[14] Although biomass-based hard carbon materials exhibit fair electrochemical properties in SIBs, the low initial coulombic efficiency and the weak cycling performance hinder the commercial application of the hard carbon-based anode materials for SIBs.[15]

Here, a novel top-down strategy is proposed to regulate the pore structure of cypress-derived hard carbon (WC-1100) *via* appropriate chemical pre-treatment and relatively low temperature carbonization for Na-ion storage. The chemical removal of lignocellulosic and hemicellulose components from the wood chips, combined with a high-temperature carbonization process, enable the rearrangement and empowerment of the carbon atoms, which, after high-temperature carbonization, contributes to the formation of closed pores, thereby increasing capacity. Cypress sawdust was treated with a chemical process followed by carbonation, which is shown in ESI.† Scanning electron microscopy (SEM) images show that the surface of WC-X (WC-900, 1100, 1300) is covered with raised structures like water droplets (Fig. S1†). Transmission electron microscopy (TEM) and high-resolution TEM were conducted to investigate the microstructure of hard carbon sample formed at various temperatures. As shown in Fig. 1a, b and S2,† such irregularly shaped carbon blocks are characterized by rough surfaces and porosity. HRTEM images (Fig. 1b, S2b and d†) indicates an abundance of short-range ordered graphite microcrystalline domains within the three materials, arranged in an irregular and random stack, creating an intricate network of pores within its hard carbon structure (*e.g.*, red circles in Fig. 1b). These pores amplify the material's specific surface area, facilitating

[a]*School of Ecology and Resource Engineering, Wuyi University, Wuyishan 354300, P. R. China*

[b]*Institute for Energy Research, Jiangsu University, Zhenjiang 212013, P. R. China. E-mail: jblian@ujs.edu.cn*

[c]*College of Science and Engineering, Flinders University, Bedford Park, South Australia 5042, Australia. E-mail: gujie.qian@flinders.edu.au*

† Electronic supplementary information (ESI) available: Experimental details, SEM images, and electrochemical results. See DOI: https://doi.org/10.1039/d4ra08080g

‡ Y. Zhou and M. X. Cen contributed equally to this work.

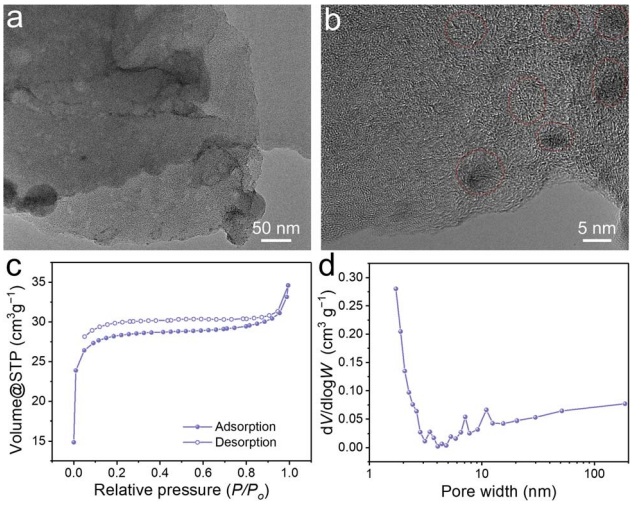

Fig. 1 (a) TEM and (b) HRTEM images of the WC-1100. (c) Nitrogen adsorption–desorption isotherm and (d) pore width distribution of WC-1100 samples.

electrolyte penetration and ion intercalation, thereby enhancing performance.

Fig. 1c and d exhibits the N_2 adsorption/desorption isotherm and pore size distribution curve of WC-1100, which further confirms abundant hierarchical pores observed in TEM images. Fig. 1c displays an obvious combination of type I and IV isotherms profile.[16] Within the low relative pressure region (P/P_0 = 0–0.1), the isotherm conspicuously manifests the hallmarks of a microporous structure. Moreover, a well-defined hysteresis loop spanning the mid-to-high relative pressure range (P/P_0 = 0.1–0.99) is observed, characteristic of a type IV isotherm, firmly illustrating the prevalence of mesopores within the sample. The pore volume and average pore size is measured as 0.57 $cm^3\ g^{-1}$ and 0.58 nm (Fig. 1d), which are tied to the inherent surface characteristics of the wood precursor, particularly its vertical pore network and microporous architecture. In addition, the Brunauer–Emmett–Teller (BET) specific surface area of WC-1100 is calculated as 108.6 $m^2\ g^{-1}$. After the precursor is treated to remove lignin and hemicellulose, the wood becomes enriched with crystalline cellulose and devoid of hemicellulose. This not only effectively reduces the specific surface area but also contributes to the increased proportion of sp^2-bonded carbon in the derived carbon material, as crystalline cellulose is more prone to forming graphite-like layered structures during pyrolysis, which are predominantly composed of sp^2-bonded carbon.[17] Consequently, the aforementioned changes help to minimize side reactions between the electrode and the electrolyte. Hence, the low specific surface area with hierarchical pores would facilitate efficient electrolyte penetration, drastically reducing the Na^+ transport distance and adequately exposing active sites for Na^+ storage, thereby enhancing overall performance.[18]

As shown in Fig. 2a, XRD analysis of the WC-900, WC-1100, and WC-1300 samples consistently display characteristic peaks indicative of amorphous carbon, prominently manifested by two broadened peaks centered at approximately $2\theta = 23°$ (002) and $2\theta = 43°$ (100). These peaks are attributed to the diffraction from the (002) and (100) lattice planes of carbon, respectively, and are hallmarks of the typical hard carbon structure. Despite the overall similarity in the XRD patterns among WC-900, WC-1100, and WC-1300, a closer inspection reveals a subtle shift in the position of the (002) peak towards higher 2θ angles with increasing carbonization temperature. This shift signifies a reduction in interlayer spacing, a direct consequence of structural evolution during the carbonization process. The central positions of the (002) peaks for WC-900, WC-1100, and WC-1300 are determined to be 23.5°, 23.7°, and 24.3°, respectively. Based on Bragg's equation ($n\lambda = 2d \sin\theta$), the average interlayer spacing d(002) for the WC-900, WC-1100, and WC-1300 samples has been calculated to be 0.38 nm, 0.37 nm, and 0.36 nm, respectively. The decrement in these values provides further corroboration for the conclusion that interlayer spacing gradually decreases with increasing carbonization temperature. This phenomenon can be attributed to the rearrangement of carbon atoms and the modulation of interlayer interaction forces during the carbonization process.

Raman spectrum analysis was conducted to investigate he structural characteristics of samples. Two characteristic peaks were observed, corresponding to the D (1350 cm^{-1}) and G band (1580 cm^{-1}), whereas the disordered degree of carbon can be determined by the intensity ratio of D band to G band (I_D/I_G).[19] An increase in the ID/IG ratio from 1.06 to 1.20 was observed with increasing pyrolysis temperatures (Fig. 2b), indicating that the highly crystalline cellulose undergoes a process akin to melting as the carbonization temperature increases, forming a graphite-like layer that subsequently contracts, leading to an increase in the number of enclosed pores.[12,20]

FTIR analysis (Fig. 2c) was further applied to confirm surface functional groups of the WC-1100. The stretching vibrations of O–H (3446 cm^{-1}), –CH_2 (2928 cm^{-1}), C=C (1617 cm^{-1}), C–O (1385 cm^{-1}) and C–O (1072 cm^{-1}) are detected in accordance with an earlier study.[21] These findings underscore the chemical composition and structural features of the WC-1100 sample, elucidating the presence of hydroxyl, alkyl, olefinic, carbonyl, and ether groups, respectively.

The Na^+ storage behavior of hard carbon samples is tested by galvanostatic charge/discharge (GCD), cyclic voltammetry (CV), and electrochemical impedance spectroscopy (EIS) analyses. Fig. 3a exhibits the charge–discharge profiles of WC-900, WC-1100, and WC-1300, characterized by a slope region above 0.1 V and a plateau region below 0.1 V. In Fig. 3b, the discharge capacities at the plateau region (<0.1 V) for the second cycle reach 242, 307, and 264 mA h g^{-1}, respectively, for these three samples. Notably, the high plateau capacity of WC-1100 can be attributed to its abundant closed pores and optimized interlayer spacing. In line with the proposed adsorption/intercalation mechanism, the plateau capacity arises from the embedding of Na^+ ions into the distorted pseudo-graphitic domains of the hard carbon when the voltage drops below 0.1 V, a phenomenon analogous to Li^+ ions insertion into graphite. Moreover, all three samples demonstrate remarkable rate capabilities (Fig. 3c). Among them, WC-1100 exhibits the best performance,

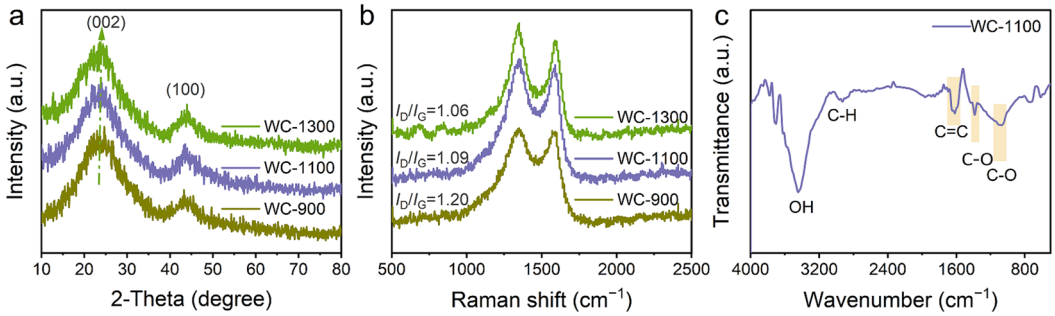

Fig. 2 (a) XRD and (b) Raman spectra of WC-900, WC-1100 and WC-1300 samples. (c) FTIR spectrum of the WC-1100.

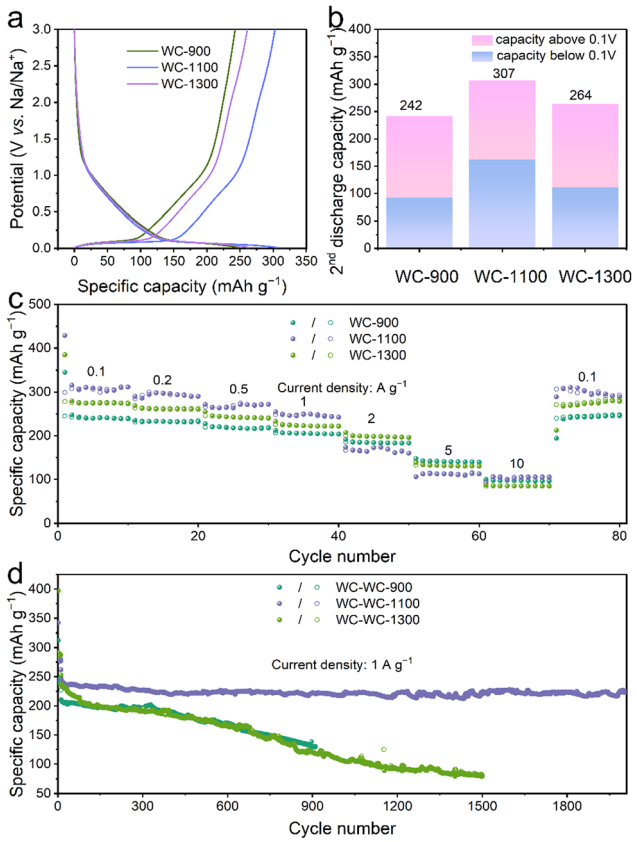

Fig. 3 (a) Galvanostatic discharge–charge profile of the 2nd cycle at 0.1 A g^{-1}, (b) the specific capacity contributions of the platform region <0.1 V and the ramp region >0.1 V are based on the discharge–charge curve of the second cycle, (c) rate performance, (d) cycling performance of the WC-900, WC-1100, and WC-1300 at 1.0 A g^{-1}.

maintaining reversible capacities of 307.5, 297.2, 274.6, 248.8, 172.6, 112.5, and 105.1 mA h g^{-1} at various current densities ranging from 0.1 to 10.0 A g^{-1}. Notably, even when the current density is returned to 0.1 A g^{-1}, its specific capacity recovers nearly to the initial level, confirming the electrode material's exceptional rate capability coupled with good reversibility. At a high current density of 1.0 A g^{-1}, after 2000 cycles (as shown in Fig. 3d), WC-1100 exhibits outstanding long-cycle stability with a capacity retention rate of 91.7% and a capacity of 242.5 mA h g^{-1}, underscoring its remarkable durability. In this study, the initial coulombic efficiencies (ICE) of WC-900, WC-1100, and WC-1300 were 76.8%, 82.5%, and 72.2%, respectively. The irreversible capacity loss is attributed to electrolyte decomposition and the formation of a solid electrolyte interface (SEI).[22] WC-1100 exhibits a relatively high Initial Coulombic Efficiency (ICE), indicating minimal charge loss during the initial cycle. Based on the TEM images of WC-1100, it has a rich pore structure. These unique pore structures are of great significance for enhancing the electrochemical performance of WC-1100. During the initial cycle, these microstructural characteristics may not only influence the formation process of the SEI, promoting the formation of a thinner and more stable structure, but also have complex interrelationships with other irreversible reactions within the system. Fig. S3† shows the CV curves and GCD profiles of the initial three cycles of WC-900, WC-1100, and WC-1300 at a scan rate of 0.1 mV s^{-1} and a current density of 0.1 A g^{-1}, respectively. The CV curves of the three hard carbon electrodes appear to be similar, suggesting a comparable sodium storage mechanism. Additionally, the excellent repeatability of these CV curves indicates a highly reversible Na^+ intercalation and deintercalation process within the hard carbon structure.[8] Within the 0.01–3.0 V potential window, all electrodes distinctly display a redox peak pair, reinforcing the successful *in situ* creation of abundant porous structures during chemical synthesis. These pores augment active sites for Na^+ intercalation/deintercalation, effectively boosting plateau-region capacity.[8,20]

In general, the Na^+ storage capacity involves capacitive and diffusion-controlled mechanisms. To explore the Na^+ storage dynamics of the WC-1100, CV tests were conducted at scanning rates from 0.2 to 1.2 mV s^{-1} (Fig. S4†). Using the power law equation (eqn (1)),[23] *b* values for peaks A and B of WC-1100 were calculated to be 0.66 and 0.70, respectively. *b* value of 1.0 indicates that the capacity primarily originates from the surface pseudo-capacitance effect, while *b* value near 0.5 indicates diffusion-controlled electrochemical reactions.[23] This manifests the significant contribution of both capacitive and diffusion-controlled reactions in the Na^+ storage process of WC-1100.

$$i(V) = av^b \quad (1)$$

Here, *a* is a proportional constant, and the *b*-value is a key parameter that describes the Na^+ storage behaviour. When the

b-value equals 1.0, it indicates that the capacity mainly originates from the surface pseudocapacitive effect; when the *b*-value approaches 0.5, it suggests that the electrochemical reaction is primarily controlled by diffusion.

EIS measurement was further employed to investigate electron transport and Na^+ dynamics (Fig. 4). In the Nyquist plot (Fig. 4a), the semicircle diameter signifies the magnitude of charge transfer resistance (R_{ct}), while the slope of the linear region reflects the Warburg impedance, tied to ion diffusion processes in the electrolyte.[24] The WC-900, WC-1100, and WC-1300 electrodes exhibit compact semicircles, indicative of low R_{ct} values of 10.0 Ω, 7.8 Ω, and 5.1 Ω, respectively, demonstrating superior electronic conductivity. According to the linear regression analysis results (Fig. 4b), the Warburg coefficients (σ) for WC-900, WC-1100, and WC-1300 were determined to be 29.55, 22.17, and 17.03 ohm $s^{-1/2}$, respectively. Based on the calculated σ (eqn (2)),[25] the D_{Na^+} values for the WC-900, WC-1100, and WC-1300 electrode materials were determined to be 2.21×10^{-10}, 2.94×10^{-10}, and 3.83×10^{-10} cm^2 s^{-1}, respectively.

$$D_{Na^+} = R^2T^2/2A^2n^4F^4C^2\sigma^2 \quad (2)$$

This significant improvement is attributed to the effective chemical regulation strategy employed, which efficiently reduced lignocellulose and hemicellulose components in the cypress wood, facilitating the formation of porous structures. Consequently, these porous structures accelerated the rapid diffusion of Na^+ within the bulk phase, endowing the electrode materials with exceptional electronic transfer and ionic diffusion behaviours.

The galvanostatic intermittent titration technique (GITT) was used to investigate dynamic behavior Na^+ diffusion (D_{Na^+}) of WC-900, WC-1100 and WC-1300 electrodes (Fig. 4c and d).

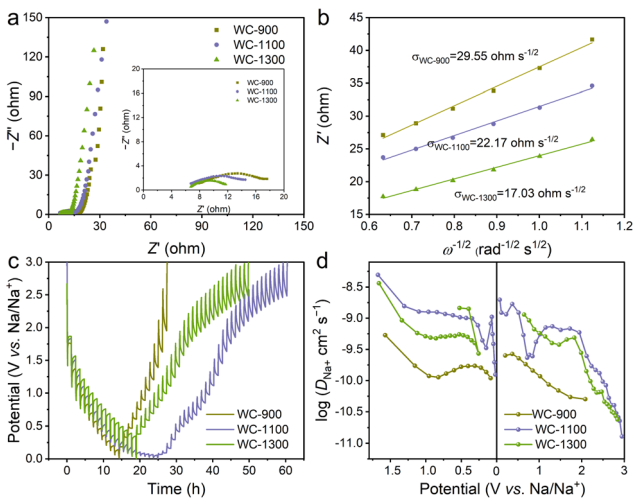

Fig. 4 (a) Nyquist plots, (b) Warburg value, (c) GITT profiles, and (d) Na^+ diffusion coefficients of the WC-900, WC-1100, and WC-1300, respectively.

The corresponding diffusion coefficients of Na^+ were calculated using the following formula:[26]

$$D_{Na^+} = 4(m_BV_M\Delta E_S)^2/\pi\tau(M_BS\Delta E_\tau)^2 \quad (3)$$

During the sodium insertion and extraction, the result of Fick's second law revealed that WC-1100 and WC-1300 showed remarkably high Na^+ diffusion coefficients (the order of 10^{-9} cm^2 s^{-1}). Notably, the WC-1100 sample exhibited a higher D_{Na^+} within the high-potential slope region (above 0.1 V), consistent with EIS results. This is primarily caused by chemical pretreatment and optimized carbonization, which enhanced Na^+ diffusion in hard carbon, notably in the high-potential region, facilitating rapid and reversible Na^+ processes crucial for battery performance. During Na^+ insertion, D_{Na^+} decreases markedly in the low-potential plateau due to slower diffusion in pseudo-graphitic regions and micropore filling, contrasting with faster diffusion in the high-potential slope. Moreover, during Na^+ insertion, D_{Na^+} values consistently decrease in the low-potential plateau (below 0.1 V), reaching a minimum near 0.01 V. This indicates slower Na^+ diffusion during intercalation/deintercalation in pseudo-graphite regions and micropore filling at low potentials, whereas faster diffusion occurs in the high-potential slope region.

Conclusions

In summary, we have successfully synthesized porous hard carbon from renewable and cost-effective cypress sawdust through a simplified, low-energy chemical pretreatment. The rich pore structure and tailored interlayer spacing of the resulting WC-1100 electrode facilitate high sodium ion storage capacity and efficient diffusion, yielding exceptional electrochemical performance: a reversible capacity of 307 mA h g^{-1} at 0.1 A g^{-1}, high ICE of 82.5%, and outstanding cycling stability (242.5 mA h g^{-1} after 2000 cycles at 1.0 A g^{-1}). This green and cost-effective chemical treatment strategy for optimizing pore structures offers a novel approach to fabricating high-performance hard carbon anodes, paving the way for producing low-cost, high-performance negative materials for advanced energy storage devices.

Data availability

The data supporting this article have been included as part of the ESI.†

Author contributions

J. B. L. conceived the idea and supervised the project. M. X. C., Y. Q. L., Y. Zhang, C. L. P. designed and performed the experiments and processed the data. Y. Zhou wrote the paper. W. J. Z., J. P. H., G. J. Q., and J. B. L. discussed and revised the paper.

Conflicts of interest

There are no conflicts to declare.

Acknowledgements

This research was funded by the National Nature Science Foundation of China (21706103), Natural Science Foundation of Fujian Province (2020J05221), the High-level Talent Scientific Research start-up program funded by China Wuyi University (YJ202108). The authors would like to thank shiyanjia lab for the support of HRTEM test.

Notes and references

1 J. B. Lian, G. Subburam, S. A. El-Khodary, K. Zhang, B. B. Zou, J. Wang, C. Wang, J. M. Ma and X. J. Wu, *J. Am. Chem. Soc.*, 2024, **146**(12), 8110–8119.
2 Z. Zhu, T. Jiang, M. Ali, Y. Meng, Y. Jin, Y. Cui and W. Chen, *Chem. Rev.*, 2022, **122**, 16610–16751.
3 Y. Tian, G. Zeng, A. Rutt, T. Shi, H. Kim, J. Wang, J. Koettgen, Y. Sun, B. Ouyang and T. Chen, *Chem. Rev.*, 2020, **121**, 1623–1669.
4 X. Chen, J. Tian, P. Li, Y. Fang, Y. Fang, X. Liang, J. Feng, J. Dong, X. Ai and H. Yang, *Adv. Energy Mater.*, 2022, **12**, 2200886.
5 Y. Fang, D. Luan, S. Gao and X. W. Lou, *Angew. Chem., Int. Ed.*, 2021, **60**, 20102–20118.
6 Y. Li, Y. Lu, C. Zhao, Y.-S. Hu, M.-M. Titirici, H. Li, X. Huang and L. Chen, *Energy Storage Mater.*, 2017, **7**, 130–151.
7 X. Yin, Z. Lu, J. Wang, X. Feng, S. Roy, X. Liu, Y. Yang, Y. Zhao and J. Zhang, *Adv. Mater.*, 2022, **34**, 2109282.
8 Y. Li, Y. S. Hu, M. M. Titirici, L. Chen and X. Huang, *Adv. Energy Mater.*, 2016, **6**, 1600659.
9 N. Sun, H. Liu and B. Xu, *J. Mater. Chem. A*, 2015, **3**, 20560–20566.
10 M. Dahbi, M. Kiso, K. Kubota, T. Horiba, T. Chafik, K. Hida, T. Matsuyama and S. Komaba, *J. Mater. Chem. A*, 2017, **5**, 9917–9928.
11 J. Wang, L. Yan, Q. Ren, L. Fan, F. Zhang and Z. Shi, *Electrochim. Acta*, 2018, **291**, 188–196.
12 Y. Li, Y. Lu, Q. Meng, A. C. Jensen, Q. Zhang, Q. Zhang, Y. Tong, Y. Qi, L. Gu and M. M. Titirici, *Adv. Energy Mater.*, 2019, **9**, 1902852.
13 D. Damodar, S. Ghosh, M. U. Rani, S. K. Martha and A. S. Deshpande, *J. Power Sources*, 2019, **438**, 227008.
14 L. A. Berglund and I. Burgert, *Adv. Mater.*, 2018, **30**, 1704285.
15 J. Jiao, C. Yi, X. Qiu, D. Yang, F. Fu and W. Liu, *Green Chem.*, 2024, **26**, 6643–6655.
16 J. Wang, S. A. El-Khodary, D. H. Ng, S. Li, Y. Cui, B. Zou, X. Liu and J. Lian, *J. Phys. Chem. Lett.*, 2022, **13**, 7273–7279.
17 Z. Tang, R. Zhang, H. Y. Wang, S. Y. Zhou, Z. Y. Pan, Y. C. Huang, D. Sun, Y. G. Tang, X. B. Ji, K. Amine and M. H. Shao, *Nat. Commun.*, 2023, **14**, 6024.
18 G. Subburam, K. Ramachandran, S. A. El-Khodary, B. B. Zou, J. Wang, L. L. Wang, J. X. Qiu, X. H. Liu, D. H. L. Ng and J. B. Lian, *Chem. Eng. J.*, 2021, **415**, 129012.
19 S. A. El-Khodary, K. Zhang, B. B. Zou, G. Subburam, Y. Zhang, J. N. Huang, J. B. Lian, Y. Zhou, C. Wang and X. J. Wu, *CCS Chem.*, 2024, DOI: **10.31635/ccschem.024.2024044**.
20 D. Saurel, B. Orayech, B. Xiao, D. Carriazo, X. Li and T. Rojo, *Adv. Energy Mater.*, 2018, **8**, 1703268.
21 L. Wang, M. Cen, S. A. El-Khodary, K. Ramachandran, J. Huang, Y. Cui, D. H. L. Ng, C. Wang and J. Lian, *Chem.–Eur. J.*, 2022, **28**, e202202358.
22 H. An, Y. Li, Y. Gao, C. Cao, J. Han, Y. Feng and W. Feng, *Carbon*, 2017, **116**, 338–346.
23 S. Alvin, C. Chandra and J. Kim, *Chem. Eng. J.*, 2021, **411**, 128490.
24 S. Hao, L. Zhang, X. Wang, G. Zhao, P. Hou and X. Xu, *Energy Fuels*, 2021, **35**, 12628–12636.
25 X. Wang, H. Hao, J. Liu, T. Huang and A. Yu, *Electrochim. Acta*, 2011, **56**, 4065–4069.
26 H. Chen, N. Sun, Q. Zhu, R. A. Soomro and B. Xu, *Adv. Sci.*, 2022, **9**, 2200023.